A computational approach for electrochemical Surface-Enhanced Raman Scattering. Key role of the surface charges and synergy between electromagnetic and charge-transfer enhancement mechanisms

Daniel Aranda,[*,†,‡] Francisco García-González,[‡] Francisco José Avila Ferrer,[‡] Isabel López-Tocón,[‡] Juan Soto,[‡] and Juan Carlos Otero[*,‡]

†*Instituto de Ciencia Molecular (ICMol), Universidad de Valencia, Catedrático J. Beltrán 2, 46980, Paterna, Valencia, Spain*

‡*Andalucía Tech, Facultad de Ciencias, Departamento de Química Física, Universidad de Málaga, 29071-Málaga, Spain*

E-mail: daniel.aranda@uv.es; jc_otero@uma.es

Abstract

We present a computational approach for electrochemical Surface-Enhanced Raman Scattering (EC-SERS). The surface excess of charge induced by the electrode potential (V_{el}) was introduced by applying an external electric field to a set of clusters $[Ag_n]^q$ with (n,q) of (19,±1) or (20,0) on which a molecule adsorbs. Using DFT/TD-DFT calculations, these metal-molecule complexes were classified by the adsorbate partial charge, and the main V_{el}-dependent properties were simultaneously studied with the aid of vibronic resonance Raman computations. Namely, changes on the vibrational wavenumbers, relative intensities and enhancement factors for all SERS mechanisms: chemical or nonresonant, and resonance Raman with bright states of the adsorbate, charge-transfer states and plasmon-like excitations on the metal cluster. We selected two molecules to test our model, pyridine, for which V_{el} has a remarkable effect, and 9,10-bis((E)-2-(pyridin-4-yl)vinyl)anthracene, which is almost insensitive to the applied bias. The results nicely reproduced most of the experimental observations, while the limitations of our approach were critically evaluated. We detected that accounting explicitly for the surface charges is key for EC-SERS models and that the highest calculated enhancement factors, up to 10^7-10^8, are obtained by interstate coupling of bright local excitations of the metal cluster and

charge-transfer states. These results highlight the importance of nonadiabatic effects in SERS and the capabilities of EC-SERS as a technique with potential to study excited state coupling by tuning the CT and plasmon-like states by manipulating V_{el}.

1 Introduction

Surface-enhanced Raman scattering (SERS) is nowadays a well established technique with great potential to characterize physicochemical properties of molecules adsorbed on surfaces.[1] However, the high complexity of the surface-adsorbate system has hindered the interpretation of experimental results with quantum chemistry models. Semiclassical models have been able to uncover the origin of the electromagnetic/plasmonic enhancement mechanism (EM),[2] but they could not provide a complete picture of other enhancement mechanisms without a proper description of the electronic structure of the surface complex.[3]

Notwithstanding the challenging nature of the SERS phenomenon, impressive theoretical advances have been carried out in just few decades after its discovery by Fleischmann, Hendra and McQuillan.[4] Amongst many achievements, it is worth to highlight the SERS selection rules derived by Lombardi and Birke, by incorporating Herzberg-Teller vibronic coupling into Albrecht expression of the transition polarizability,[5,6] and methodological advances lead by Jensen group.[7–12]

Nowadays, there is a general consensus about the sources of amplification of the Raman scattering differential cross sections and the enhancement factor (EF) order of magnitude associated with each contribution. The weakest of them typically is the static or nonresonant chemical (CHEM) contribution due to the molecular adsorption on the metal surface, with $EF_{CHEM} \sim 10^1$-10^2. Next, the enhancement due to photoinduced charge transfer (CT), with $EF_{CT} \sim 10^1$-10^4, resonances with adsorbate bright states (RR), $EF_{RR} \sim 10^3$-10^6 and finally, resonances with plasmonic excitations $EF_{EM} \sim 10^4$-10^8.[13] By combining them, experimental EFs up to 10^{14} have been reported allowing for single-molecule detection[14] and soundly establishing SERS as an ultrasensitive analytical technique. However, special care must be taken on the experimental quantification of EFs to avoid misleading results.[15]

Despite this progress on the computation of SERS properties, we currently lack a general strategy to model SERS systems. This is even more evident for the study of electrochemical SERS experiments (EC-SERS),[16] where the metal surface on which the molecule adsorbs is used as an electrode, resulting in an electrified interface. EC-SERS can provide very useful information about the effect of the applied electric potential on the interaction between molecules and charged metal surfaces, a topic of high interest in fields like electrocatalysis or surface science.[16,17] However, incorporating the surface excess of charge generated by applied potentials (V_{el}) in atomistic models is very challenging because V_{el} is a parameter of macroscopic

nature. Several computational approaches for V_{el} in combination with DFT and TD-DFT calculations have been proposed based on average density of charge on a set of small clusters,[18] external electric fields,[19] semiempirical methods,[20] partial charges on adsorbates[21] or electrolyte-based models.[22] All of them coincide on modulating the electronic structure of the metal cluster by different means so that the charge injection by adsorbate is favoured or hindered.

Theoretical investigations in EC-SERS usually focus on studying the photoinduced metal-molecule CT mechanism by reproducing the changes on the relative intensities as V_{el} varies, because V_{el} can manipulate very efficiently the energy of the excited CT states of the surface complex. As a result, other interesting properties are generally pushed into the background, like the estimation of EFs and the subtle change of the vibrational wavenumbers with V_{el}, the so called Vibrational Stark Effect (VSE).[23] VSE provides direct information on the electronic structure of the surface complex, but also allows to study intermolecular interactions in supramolecular systems and it is of interest in many fields like surface science,[24,25] enzymatic catalysis[26] or molecular electronics.[27]

To the best of the our knowledge, no computational model for EC-SERS has been able to simultaneously reproduce the three main properties that can be quantified in EC-SERS experiments, namely the voltage tuning of spectral shapes, wavenumbers and EFs of the different mechanisms. In this paper we propose a new approach for V_{el} by describing the surface excess of charge with the combined effect of charged metal clusters and external electric fields. The physical meaning for the charges is an electrified adsorption site, while the electric field implicitly models the effect of charges near to where the molecule adsorbs. To evaluate this approach, we studied two chemically related systems but with very different SERS behaviour (see Scheme 1). Pyridine (Py) is an emblematic and widely studied molecule in SERS and its spectra show a remarkable sensibility with V_{el} for both wavenumbers and intensities,[28] reason why it is very often used to test theoretical models.[19,28,29] On the contrary, the related derivative 9,10-bis((E)-2-(pyridin-4-yl)vinyl)anthracene (BP4VA), is a much more complex molecule with extended $\pi-$conjugation which shows RR processes using standard excitation lines in the visible. For BP4VA, the spectra are almost insensitive to V_{el} and few changes are observed during EC-SERS experiments.[30] Therefore, these two molecules are good candidates to evaluate the proposed computational model by estimating the three main fatures of EC-SERS experiments: VSE, relative intensities, and EF.

2 Theory

As presented in Section 1, four enhancement mechanisms can be identified in SERS according to the nature of the electronic states contributing to the transition polarizablity tensor α: i) nonresonant or static chemical

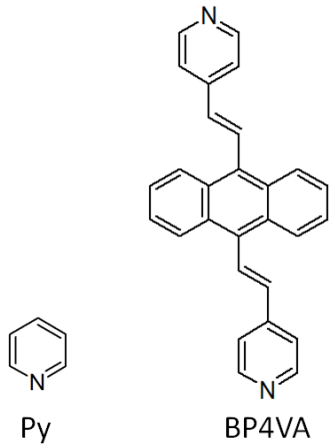

Scheme 1: Chemical structures of the molecules pyridine (left) and 9,10-bis((E)-2-(pyridin-4-yl)vinyl)anthracene (right) studied in this work.

enhancement due to the changes on the ground state polarizability when the scattering molecule adsorbs on the metal surface (α_{CHEM}), and resonance Raman processes with ii) states localized in the adsorbate (α_{RR}), iii) states localized in the metal (electromagnetic, α_{EM}), or iv) charge-transfer states (α_{CT}).[9,13] Therefore, the total transition polaribility tensor α_{SERS} can be defined as:

$$\alpha_{SERS} = \alpha_{CHEM} + \alpha_{RR} + \alpha_{CT} + \alpha_{EM} \tag{1}$$

CHEM contribution can be computed in the Placzek approximation, which is valid for non-resonance cases but can be extended also to resonances by invoking the short-time approach.[7] When the ground state is well separated from the excited states, the Born-Oppenheimer approach can be safely applied, obtaining the following expression for the Raman cross section of a vibrational mode p for perpendicular plane-polarized light and collected at 90°:[31,32]

$$\left(\frac{d\sigma}{d\Omega}\right)_{p,CHEM} = \frac{\pi^2}{\epsilon_0^2}(\tilde{\nu}_{in} - \tilde{\nu}_p)^4 \frac{h}{8\pi^2 c\tilde{\nu}_p} \frac{S_p}{45[1 - \exp(-\frac{hc\tilde{\nu}_p}{k_B T})]} \tag{2}$$

$\tilde{\nu}_{in}$ and $\tilde{\nu}_p$ are the wavenumbers of the incident radiation and of the vibrational normal mode p, while h, ϵ_0, c and k_B are Planck's constant, the vacuum permittivity, the speed of light and Boltzmann's constant, and T is the temperature. $S_p = 45a_p'^2 + 7\gamma_p'^2$ is the Raman activity,[31] a pure molecular property which does not depend on experimental conditions and is a function of the derivative of the mean isotropic polarizability a_p (also labeled as $\bar{\alpha_p}$ in the literature) and the derivative of the anisotropic polarizability γ_p, both with respect to the mass-weighted normal coordinates of mode p.[33] The differential cross sections are usually expressed in 10^{-30} cm^2, see Section 1.1 in the SI for details on units.

The resonance Raman intensities of mode p for contributions $\chi = RR, CT, EM$ can be obtained by the following expression:[32,34]

$$\left(\frac{d\sigma}{d\Omega}\right)_{p,\chi} = \frac{\pi^2}{\epsilon_0^2}(\tilde{\nu}_{in} - \tilde{\nu}_p)^4 \frac{45a_{\chi,p}^2 + 7g_{\chi,p}^2 + 5d_{\chi,p}^2}{45} \tag{3}$$

g_p and d_p are respectively the symmetric and antisymmetric anisotropic polarizabilities. Notice that $\gamma_p^2 = g_p^2 + d_p^2$ and that a_p, g_p and d_p are the so-called polarizability invariants, which are functions of the transition polarizability tensor components between initial i and final f states $\alpha_{\rho\sigma}^{fi}$ (ρ, σ = x, y, z), and are independent of the molecule orientation with respect to the incident field (see Section 1.1 in the SI for their full expression). In a time-independent framework, $\alpha_{\rho\sigma}^{fi}$, for a Raman transition between vibrational states i and f can be calculated from the Kramers-Heisenberg-Dirac (KHD) formula for scattering:[35,36]

$$\alpha_{\rho\sigma}^{fi} = \frac{1}{\hbar}\left[\sum_m \frac{\langle \mathbf{n}^{f,g}|\mu_\rho^{gk}|\mathbf{m}^k\rangle\langle \mathbf{m}^k|\mu_\sigma^{kg}|\mathbf{n}^{i,g}\rangle}{\omega_{km,gi} - \omega_{in} - i\gamma_k} + \frac{\langle \mathbf{n}^{f,g}|\mu_\rho^{gk}|\mathbf{m}^k\rangle\langle \mathbf{m}^k|\mu_\sigma^{kg}|\mathbf{n}^{i,g}\rangle}{\omega_{km,gi} + \omega_{in} - i\gamma_k}\right] \tag{4}$$

where $|\mathbf{n}^{f,g}\rangle$ and $|\mathbf{n}^{i,g}\rangle$ are the initial i and final f vibrational states of the electronic state g, $|\mathbf{m}^k\rangle$ is the m vibrational state of the electronic state k, $\mu_\beta^{gk} = \langle k|\mu_\beta|g\rangle$ is the $\beta = x, y, z$ component of the electric transition dipole moment (ETDM) between electronic states g and k, $\omega_{km,gi} = \omega_k + \omega_{v_m^k} - (\omega_g + \omega_{v_i^g})$ and it depends on the angular frequency of the electronic states g, k and their respective vibrational states v_p, v_i. ω_{in} is the angular frequency of the incident radiation and γ_k is the damping factor of the electronic state k.

In the FC approximation $\mu_\beta^{gk} = \mu_\beta^{gk}(0)$ is constant and ignoring the non-resonance term Eq. 4 becomes:

$$\alpha_{\rho\sigma}^{fi} = \frac{1}{\hbar}\left[\mu_\rho^{gk}(0)\mu_\sigma^{kg}(0)\sum_m \frac{\langle \mathbf{n}^{f,g}|\mathbf{m}^k\rangle\langle \mathbf{m}^k|\mathbf{n}^{i,g}\rangle}{\omega_{km,gi} - \omega_{in} - i\gamma_k}\right] \tag{5}$$

In these conditions $\alpha_{\rho\sigma}^{fi}$ is simply a function of i) the ρ, σ components of the ETDM, ii) the Franck-Condon (FC) factors $\langle \mathbf{n}^{f,g}|\mathbf{m}^k\rangle$ and $\langle \mathbf{m}^k|\mathbf{n}^{i,g}\rangle$, and iii) the energy difference in the denominator. This is equivalent to the resonance contribution of Albrecht A term.[5] Because the intensity is proportional to functions of $|\alpha_{\rho\sigma}^{fi}|^2$, we can expect that bright states with large displacements along the normal coordinates should have the largest contribution. On the other hand, pure CT transitions have usually dark character and vanishing contribution in the FC approximation. Therefore, the role of vibronic coupling must be considered, that is, B, C or D Albrecht terms. To properly include these effects, nonadiabatic approaches should be used but these methodologies are only available for small systems.[37] Notwithstanding this, we can obtain a qualitative prediction of which normal modes are enhanced by vibronic coupling using the perturbative Franck-Condon Herzberg-Teller (FCHT) approximation because the modes with largest transition dipole derivatives are expected to show also the strongest interstate coupling.[38]

3 Computational Details

Electronic structure calculations were performed with Density Functional Theory (DFT) and its Time-Dependent extension TD-DFT as implemented in the Gaussian16 code.[39] The long-range corrected functional CAM-B3LYP[40] has been utilized to obtain reliable excitation energies for charge-transfer states, in combination with Pople basis set 6-31+G(2d,2p)[41,42] for N, C and H atoms and the LANL2DZ core potential for Ag.[43–45] (see section 1.2 in the SI for a small benchmark on the size of the basis). Non-bonded interactions between the adsorbate and the metal complex were introduced with Grimme GD3 dispersion corrections,[46] and the charge on molecular fragments, i.e., metal cluster and adsorbate, were computed with the CM5 model.[47] See Section 1.3 on the SI for restrictions on the optimization of structures and the displacement vectors of the relevant normal modes.

Nonresonant intensities, expressed as differential cross sections, were computed with Eq. 2 setting T = 300K and the incident radiation wavelength to = 514.5 nm as in experiments.[28,30] Resonance Raman intensities for the metal-pyridine systems were calculated with the time-independent expression of Eq. 3 as implemented in the code FCclasses3[34,48,49] with the Vertical Gradient model[50] in combination with the FC and FCHT approximations for the ETDM.[51,52] To ensure convergence for BP4VA, much larger in size, the RR spectra were calculated with an independent derivation of a time-dependent expression for the transition polarizabilities, similar to what reported by Baiardi, Bloino and Barone,[53] and recently implemented in a development version of FCclasses3.[48] For each state, the RR spectra the incident wavelength was set equal to its vertical energy in order to obtain an upper bound for the intensity of that state, i.e., $\omega_{km,gi} = \omega_{in}$. When several bright states were close in energy, the total spectrum was obtained by adding the contributions to $\alpha^{fi}_{\rho\sigma}$ components before computing the intensity to take into account interference effects. Such $\alpha^{fi}_{\rho\sigma}$ components were computed by setting the energy of the incident radiation equal to the excitation energy of most intense state for all the close-lying states. Normal modes of the metal cluster were projected out of the vibrational space,[54,55] and the damping factor $\hbar\gamma_k$ was set to 800 cm^{-1} ($\sim$ 0.1 eV) as reported in the literature for pyridine.[29] This parameter has been related to the strength of the metal-adsorbate interaction,[56] therefore, the same value of γ_k was utilized for BP4VA because it also attaches to the metal surface through a pyridyl group. All stick-line transitions were convoluted with a Lorentzian of half-width at half-maximum of 5(10) cm^{-1} for Py(BP4VA).

4 Molecular Model

The proposed model for the metal-molecule surface complex in EC-SERS is based on the $[Ag_{20}]^0$ tetrahedral cluster studied by Zhao, Jenssen and Schatz[29] to which we incorporated the effect of V_{el} in the electronic structure. In a macroscopic perspective, V_{el} modifies the surface excess of charge on the metal, resulting in a reconstruction of the electrochemical double layer structure. Therefore, the adsorbate is subject to a modification of the chemical and physical interactions originated by the surface charges. To introduce the effect of the surface charges, we have considered two different approaches for a charged interface (Figure 1): a $[Ag_{20}]^0$ cluster representing a neutral adsorption site under the effect of surface charges described as an external electric field, or a charged adsorption site with charge $q = \pm 1$ in combination with external fields. To conserve the computationally convenient singlet configuration, a silver atom on the opposite side to the binding site was removed in order to minimize its impact on the electronic structure of the complex, resulting in the $[Ag_{19}A]^q$, $q = \pm 1$, A = Py, BP4VA, set of complexes. We considered the two adsorption sites studied in Ref. 29 – center of the face (S-complex) or vertex (V-complex) – to which we added the effect of V_{el} to evaluate the effect of local environment. The discussion here presented focus on the S-complexes, whereas V-complex results are shown in the SI.

The Coulomb potential generated by the electrified interface is modeled with an external electric field of magnitude $|E|$ applied perpendicularly to the adsorption site of the surface complex. The magnitude $|E|$ qualitatively mimics the density of surface charges in the proximity of the adsorption site. This surface density of charge is related to the difference between V_{el} and the potential of zero charge of the electrode (V_{PZC}), for which the surface is neutral. On the other hand, E direction accounts for an excess of positive or negative surface charges. The supramolecular complex was oriented in such a way that $+|E|$ favors the injection of electrons from the adsorbate to the metal cluster and $-|E|$ hinder it (see Figure S4). Therefore, i) the $[Ag_{20}A]^0$ complex with no external field would correspond to V_{PZC}, ii) $[Ag_{19}A]^+ + |E|$ and $[Ag_{20}A]^0 + |E|$ set of clusters model a situation where $V_{el} > V_{PZC}$, a positively charged surface, and iii) $[Ag_{19}A]^- - |E|$ and $[Ag_{20}A]^0 - |E|$ correspond to $V_{el} < V_{PZC}$, a negatively charged surface. In both cases ii) and iii) we considered the possibility of a neutral or charged adsorption site with the $[Ag_{20}A]^0 \pm |E|$ and $[Ag_{19}A]^q \pm |E|$ ($q = \pm 1$) complexes, respectively.

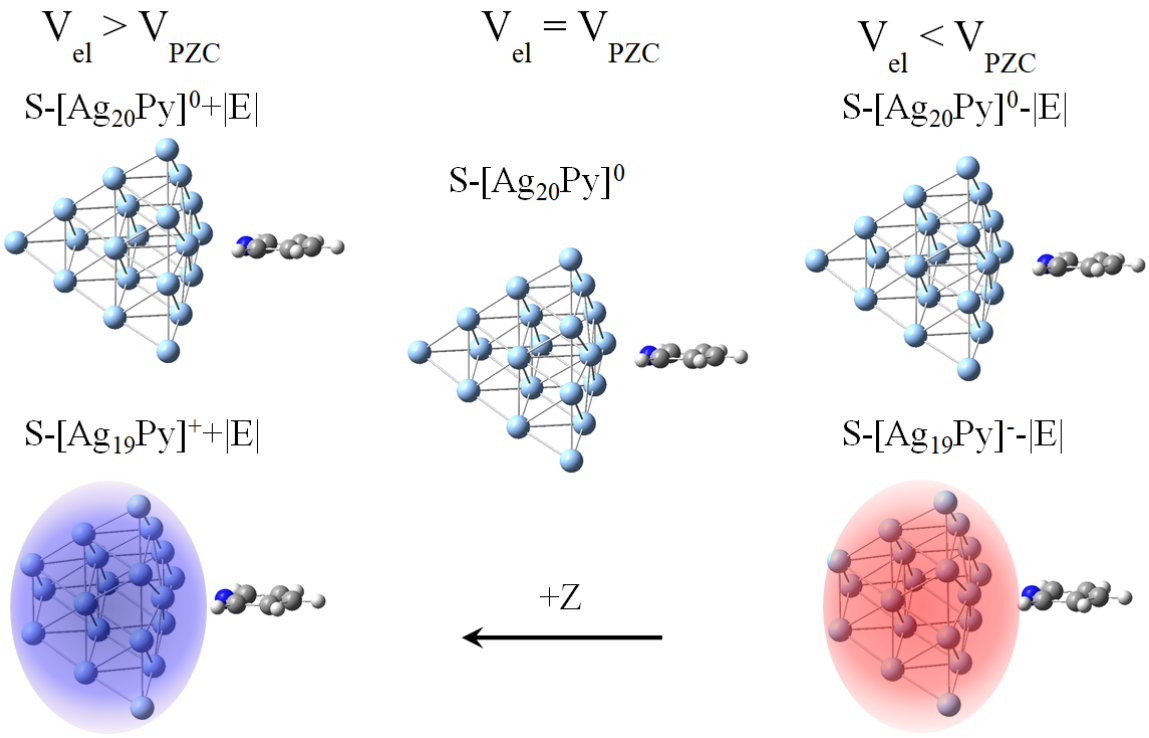

Figure 1: Molecular model for SERS proposed in this work (S-complexes). The charges on the adsorption site are explicitly included while an external electric field applied along Z-direction reproduces the effect of nearby surface charges.

5 Results

5.1 Microscopic analog to V_{el}

The comparison of computed EC-SERS spectra with experiments is not trivial because a parameter must be defined to represent V_{el} in the calculations, see SI for further details. To correlate the results obtained for clusters with different number of atoms and total charge, we selected the total charge on the adsorbate, q_A, as microscopic analog for V_{el}. For the adsorbates selected, the interaction with the metal surface arise from the charge injection of the nitrogen lone pair. This charge injection depends on the type of atom to which the adsorbate is bound (vertex, center of face, etc., see SI) and it is modulated by both q and E.

Figure 2 shows the charge of pyridine q_{Py} in the S-$[Ag_{19}Py]^+ + |E|$, S-$[Ag_{20}Py]^0 \pm |E|$ and S-$[Ag_{19}Py]^- - |E|$ series of complexes under a range of electric fields E (see Table S1 for the values). In all cases, q_{Py} and E are linearly correlated, although the negatively charged S-complexes show a slightly larger slope. Notice also that i) the neutral systems can cover a large range of q_{Py} without observing changes on the oxidation state of the adsorbate or dissociation of the complex and ii) explicit charges have a remarkable impact, shifting q_{Py} vertically ±0.05-0.07 a.u. when a positive or negative charge is added or removed to the metal cluster.

These results suggest that it is possible to relate the smooth trends observed for EC-SERS recorded at

different V_{el} to a series of q_A values obtained from several $[Ag_nA]^q \pm |E|$ complexes with (n,q) of (19,±1) or (20,0) in combination with different magnitudes and directions of E. Noteworthy, the same q_A can be reached by different models. For instance, both S-$[Ag_{19}Py]^+ + 10$ and S-$[Ag_{20}Py]^0 + 60$ complexes have $q_{Py} \sim 0.11$ a.u., while for S-$[Ag_{20}Py]^0 - 60$ and S-$[Ag_{19}Py]^- - 10$ q_{Py} = -0.01 a.u. By comparison with the experimental results we can select which combination of q and E is more meaningful.

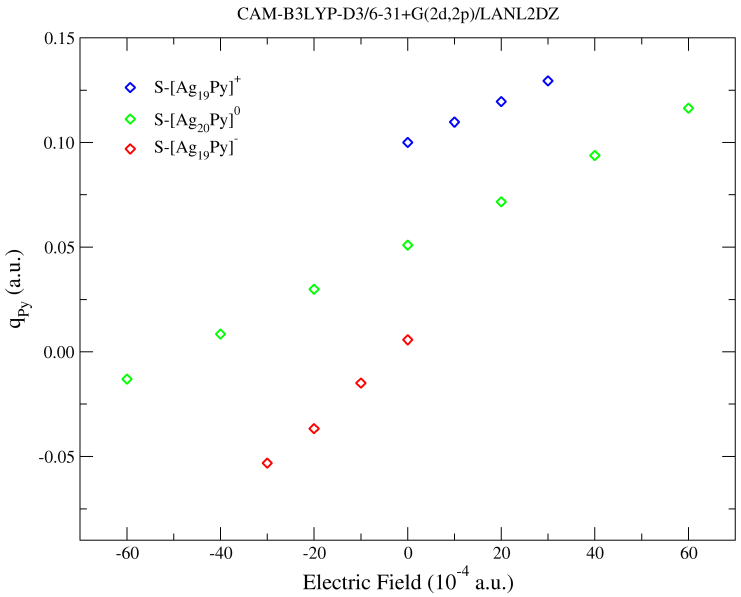

Figure 2: Dependence of the charge of pyridine q_{Py} on the external electric field E for S-$[Ag_{19}Py]^+$, S-$[Ag_{20}Py]^0$ and S-$[Ag_{19}Py]^-$ complexes. CAM-B3LYP-D3/6-31+G(2d,2p)/LANL2DZ level of theory.

5.2 Pyridine

5.2.1 Vibrational Stark Effect: Dependence of vibrational wavenumbers on V_{el}.

The EC-SERS spectra of pyridine in silver electrode are characterized by few bands (see Figure S1).[28,57] Here we focus on the a_1 vibrations that are SERS active: ring stretching (8a, Wilson notation for benzene-like normal modes[58]), CH bending (9a), ring deformation (18a), ring trigonal deformation (12), ring breathing (1) and ring deformation along the binary axis (6a), with experimental Raman shifts of 1590, 1215, 1067, 1033, 1005 and 622 cm^{-1}, respectively. See Figure S5 for displacement vectors of these vibrations, while animations can be found in SI of Ref 28. Figure 3 shows the experimental and calculated Raman shift dependence for S-complexes. Three regions can be distinguished from the experimental EC-SERS data (values against Ag/AgCl/KCl (sat) reference electrode):[28] from 0.0 V to -0.4 V the Raman shifts are roughly constant (region A), from -0.5 V to -1.0 V they show a linear dependence with V_{el} (region B) and finally, from -1.1 V to -1.4 V the dependence is also linear but with a smaller slope than in region B (region C). Notice that mode 18a shows the opposite behaviour for regions A and B, i.e, linear and constant, respectively.

q_{Py} ranges from -0.05 to 0.15 a.u. for the selected set of complexes, and nicely reproduces the Raman shift ranges and dependence on V_{el} for all the vibrational modes except for 9a, whose possible sources of disagreement are discussed in the SI. Region A is well described by the positive S-$[Ag_{19}Py]^+ + |E|$ clusters as well as by the neutral S-$[Ag_{20}Py]^0 + |E|$ complex with positive fields of E = 60, 40, 20 (in 10^{-4} a.u.), both models show little sensitivity to q_{Py} between 0.13 and 0.08 a.u (see 8a or 12 modes in Figure 3, for instance). However, calculated shifts for modes 1 and 6a show larger dependence on q_{Py} than experiments do on V_{el}. Experimental region B is also well reproduced by the S-$[Ag_{20}Py]^0 \pm |E|$ model with E = +20, 0, -20 and -40 (in 10^{-4} a.u.), except for mode 18a which shows a small slope in the calculations while remains almost constant experimentally. Finally, the results for the negatively charged S-$[Ag_{19}Py]^- - |E|$ complex reproduce well the smaller slope of region C recorded from -1.0V to -1.4V. These results are in line with what reported in Ref. 28 for the charged clusters model and that provided the correct qualitative behaviour but the ranges were overestimated. The new results presented in Figure 3 are almost in quantitative agreement for most of the vibrational normal modes, which is a notable improvement with respect to other models.

Notice that shifts for the S-$[Ag_{20}Py]^0 - 60$ model with q_{Py}= -0.01 a.u. are out of the trend for most of the cases, while the results of the S-$[Ag_{19}Py]^- - 10$ complex with similar q_{Py} seem to fit better (see Table S1). This suggest that very negative fields on a neutral adsorption site may have no physical meaning because the clusters over the metal surface still behave as conductors or semiconductors. Therefore, once the number of surface charges represented by the magnitude of E is large enough, the adsorption site becomes charged as well. According to our results, the best combination of clusters to reproduce the experimental VSE of Py

would be the all the considered $[Ag_{19}Py]^{+} + |E|$ set of clusters, $[Ag_{20}Py]^{0} \pm |E|$ with fields +20,0, -20 and -40, and the $[Ag_{19}Py]^{-} - |E|$ series.

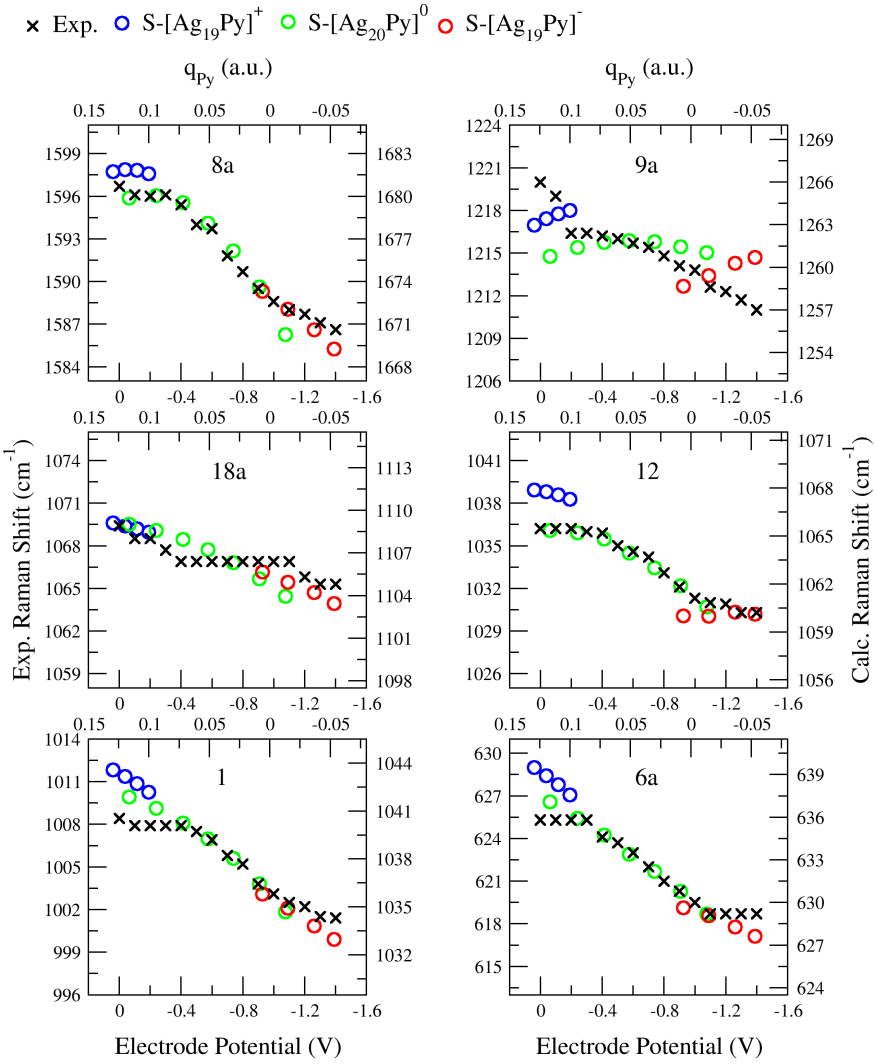

Figure 3: Raman shift electrode potential dependence of the main a_1 normal modes of pyridine. The Y-axis represents the experimental (left) and calculated (right) Raman shift, and in all cases the range is 22 cm^{-1}. The calculated Raman shift range is selected to fit as best as possible with the experimental results. The X-axes show the experimental electrode potential applied (bottom) and the calculated charge on pyridine (top). Calculated results for S-complexes. CAM-B3LYP-D3/6-31+G(2d,2p)/LANL2DZ level of theory. Excitation wavelength of 514.5 nm for experiments, data from Ref. 28.

The quite good agreement between experimental and calculated SERS vibrational shifts allows us to discuss some electrochemical properties. According to our results, the neutral surface model $[Ag_{20}Py]^{0}$ would correlate to V_{el} = -0.6V, slightly shifted towards more positive voltages than in macroscopic experiments on bare polycrystalline silver electrode where V_{PZC} ranges between -0.7 V and -0.9 V.[59] This small positive difference can be due to the adsorption of pyridine, which is a donor ligand and the injected charge can partially

neutralize the surface excess of charge, resulting in a shift of V_{el} to more positive potentials. Therefore, in the following it is assumed that in the specific conditions of the discussed SERS spectra of pyridine adsorbed on a roughened electrode, $V_{PZC} \sim$ -0.6V. Although a direct comparison of microscopic properties obtained with atomistic models and the macropscopic V_{el} must be taken with caution, this qualitative correspondence is interesting because electrochemical estimations of V_{PZC} are challenging experimentally.[60]

Similarly, our results suggest that the adsorption site, i.e. the SERS "hot spot", may become negatively charged for $V_{el} \sim$ -1.0V in this specific experimental set up, justifying the change on slopes from region B to C discussed before. In the range between -0.6V to -1.0V our model suggests that the adsorption site is neutral although there is a negative excess of charge on the surface. This hypothesis is also supported by experimental observations on silver electrodes for molecules more weakly attached to the surface. Pyrazine or anionic adsorbates like carboxilic acid derivatives,[61,62] desorb from the metal surface for V_{el} values similar to what here proposed, about -1.0V. These results highlight once again that EC-SERS is a very powerful technique in surface science and its combination with electronic structure calculation can provide valuable information to study the complex electrochemical phenomena taking place in charged surfaces.

5.2.2 Spectra and enhancement factors

Nonresonant Raman spectra are analyzed in the SI and the results nicely reproduce some of the most relevant experimental features. Our estimates for EF_{CHEM} are of 1.2 to 2.0 with respect to isolated pyridine and fall in the range previously reported in the literature: a factor of 2-4 for S-$[Ag_{20}]^0$ and twice this value for V-$[Ag_{20}]^0$.[29]

Next, we studied resonances with specific states of the systems. Pyridine local excitations are very high in energy (>6 eV)[63] so we focused on the other two mechanisms, EM and CT. In the atomistic model here proposed the EM contribution arises from bright states localized in the metal cluster. In Figure S10 we represented the oscillator strength of all the electronic transitions of the S-complexes. For most of the neutral and positively charged clusters there are only three strongly absorbing states in the region 3.6-3.8 eV, while for negatively charged clusters and neutral ones with strong and negative fields, many bands have similar oscillator strength, so a larger number of states must be considered. This is due to the mixing of bright local excitations of the metal with CT states.

In Figure 4 we compared experimental SERS spectra and calculated RR spectra of bright states for matching pairs of V_{el} and q_{Py} according to the vibrational wavenumber trends showed in Figure 3. For instance, the S-$[Ag_{20}Py]^0$ cluster is related to $V_{el} \sim$ -0.6V. A systematic discussion of relevant states for all models is given in Section 2.4 in the SI. A detailed analysis of the calculated EC-SERS spectra is challenging and, therefore, the discussion will be organized according to the total charge of the cluster q and direction of E, starting from the complexes with larger q_{Py}.

Firstly, for most of the positively charged S-$[Ag_{19}Py]^+ + |E|$ complexes shown in Figure S14, the EM spectra are dominated by bright plasmon-like excitations on the metal cluster polarized in the Z-direction (state S51). These spectra resemble their NR counterparts and agree with the experimental results for the corresponding V_{el} except for the enhancement of mode 6a, limitation that has also been observed in other works using the $[Ag_{20}]^0$ cluster and ascribed to the small size of the cluster with respect to true nanostructured electrodes or nanoparticles.[29] Secondly, for $[Ag_{20}Py]^0 + |E|$ clusters and also S-$[Ag_{20}Py]^0$, the calculated EM spectra greatly differ from the NR and the corresponding experimental spectra (see Figure S12). The discussion on these discrepancies is extended in the SI, but it is apparently related to the small changes on Py electronic density for these states. Thirdly, some of the $[Ag_{20}Py]^0 - |E|$ set of clusters predict a large enhancement at 1680 cm^{-1} (1600 cm^{-1} in experiments), in agreement with the experimental region -0.7V to -0.9V associated to them. Finally, S-$[Ag_{19}Py]^- - |E|$ clusters reproduce very nicely the experimental features in the range -1.1 to -1.3V and matched with their calculated NR, i.e., strong intensity for bands 1 and 9a, and small intensity for modes 12 and 8a (see Figures S26), although the intensity of fundamental

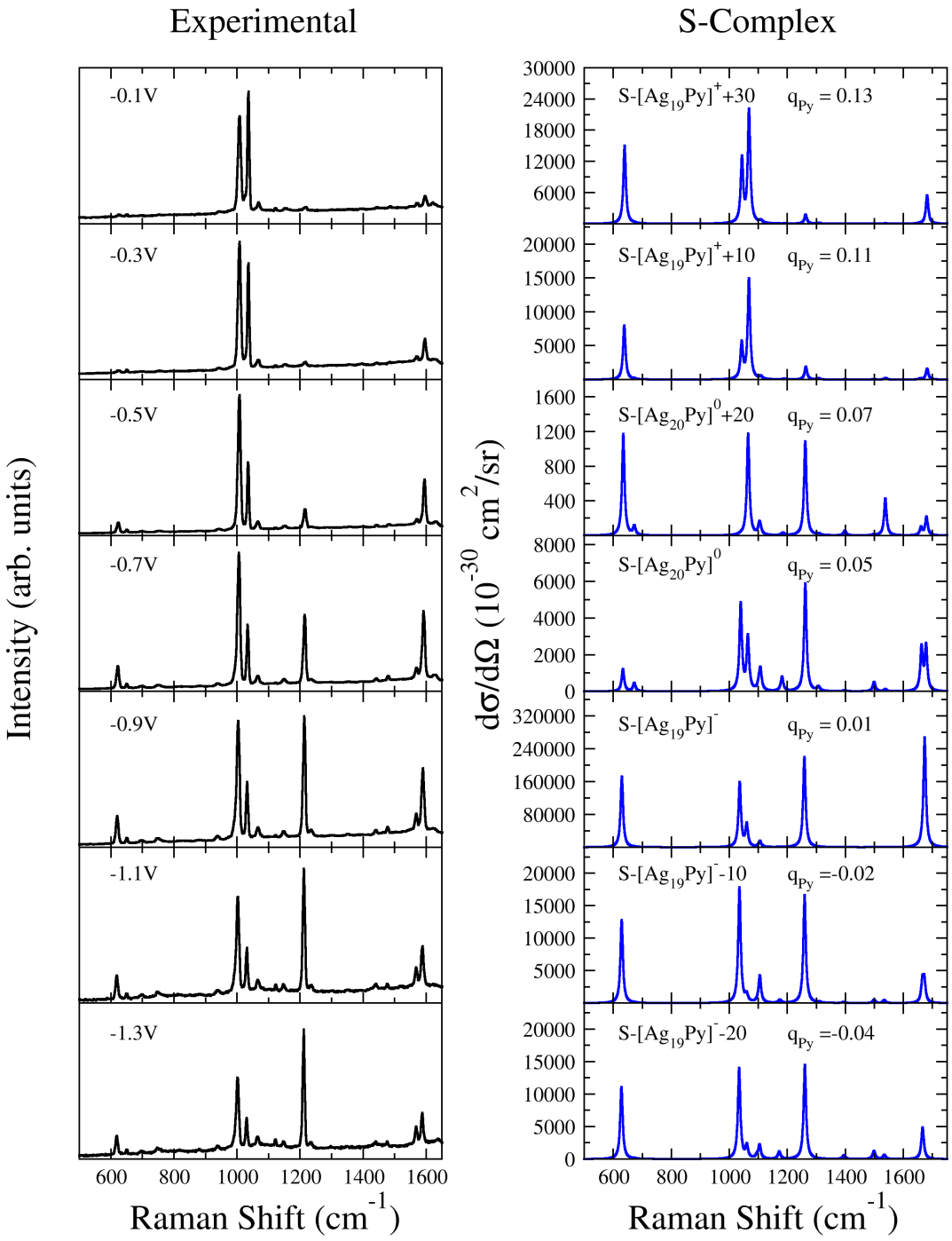

Figure 4: Experimental SERS (left) and calculated FC|VG resonance Raman spectra for the bright states (right) for matched values of V_{el} and q_{Py}. Notice that each panel has different Y-axis scale. On each row, the selected experimental and calculated systems showed similar values for the Raman shifts in Figure 3. The calculated spectra account for interference effects when several bright states were close in energy, see SI for individual spectra. Stick lines were convoluted with a Lorentzian of HWHM = 5 cm^{-1}. All E in 10^{-4} a.u. CAM-B3LYP-D3/6-31+G(2d,2p)/LANL2DZ level of theory. Experimental data from Ref. 28 with excitation line of 514.5 nm.

6a is overestimated for these models like in the positive region. Therefore, in overall terms, the proposed computational model manages to reproduce the experimental trends observed in EC-SERS for most of the V_{el} range except for $V_{el} \approx$ -0.5V for S-complexes.

Another relevant SERS parameter that can be extracted from Figure 4 are the EFs. The calculated NR of isolated pyridine showed differential Raman cross sections in the order of 10^{-31} cm^2/sr (see Figure S1). Therefore, our estimation for EF_{EM} according to Figure 4 typically ranges 10^4-10^5, in agreement with experimental observations. Noteworthy, the complex S-[Ag_{19}Py]$^-$ shows largerEF_{EM} of 10^6 and this is discussed below.

The calculated spectra for this complex is the result of adding the contribution of two bright states. The two states have identical spectral shape but different intensity because of the ETDM magnitude (see Figure S27 and Table S4), therefore, it suffices analyzing one state. Figure 5 shows the natural transition orbitals[64] (NTOs) for some selected states with large resonance Raman intensity, while the discussion of the main NTOs of the bright states for all the studied complexes is given in Section 2.4 of the SI. Noteworthy, about 40-50% of these states have a clear CT component as the virtual orbital is mainly localized in Py: for S-[Ag_{19}Py]$^-$ S69 the virtual orbital resembles to Py LUMO, of B_1 symmetry, with some minor contribution in the metal cluster. Differently, for S-[Ag_{20}Py]^0 −40 S67 the virtual orbital is Py LUMO+1, of A_2 symmetry. Therefore, we label these states as CT_0 and CT_1 states, respectively. These spectra agree well with what has been previously reported in the literature,[18,29] and the main difference between CT_0 and CT_1 is the lack of intensity on 9a band, see SI. The relative intensities calculated under resonance with the CT_0 state show the characteristic triangular-like spectral shape which has also been detected in experiments on Ni electrodes.[65]

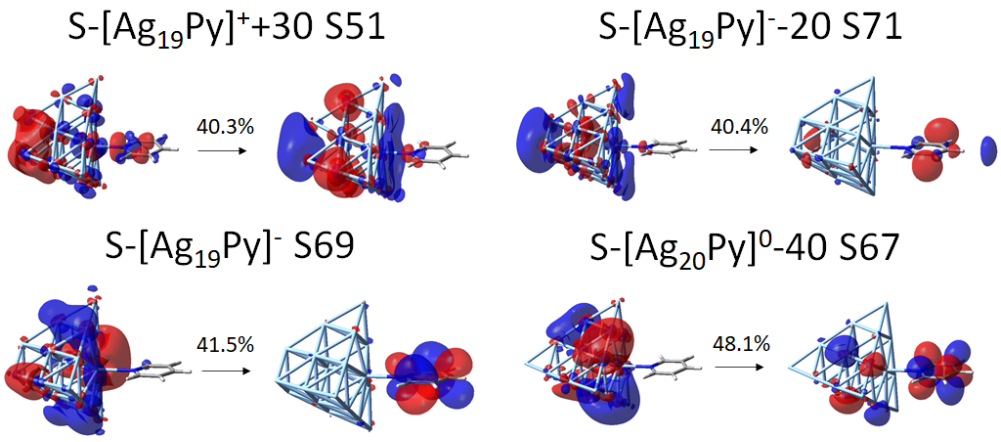

Figure 5: Natural transition orbitals (NTOs) for selected states with large resonance Raman intensity for the S-complexes. The weight of each pair of NTOs transition is showed over the arrows. All E in 10^{-4} a.u. CAM-B3LYP-D3/6-31+G(2d,2p)/LANL2DZ level of theory. Isosurface of 0.02 a.u.

Interestingly, other states with large EFs for positively and negatively charged clusters also show some

partial CT character (see Figure 5 for some examples and Figures S15-S18, S28-S31 for the full set of mixed EM/CT states of S-complexes): for S-$[Ag_{19}Py]^+ + 30$ S51 with $EF_{EM} \sim 10^5$ (and also in other positively charged S-complexes), the occupied orbital is delocalized and involves Py HOMO, while the virtual orbital is mostly localized on the metal cluster suggesting a partial molecule-to-metal CT character. Finally, for negatively charged clusters many of these states show metal-to-molecule CT character involving instead Rydberg-type molecular orbitals on Py (see S71 of S-$[Ag_{19}Py]^- - 20$ in Figure 5 for example, $EF \sim 10^5$), explaining the different spectral shapes with respect to CT_0 and CT_1 states: while the resonance with these two CT mainly enhance mode 8a, for Rydberg-type CT transitions the strongest bands are 1 and 9a. Surprisingly, the RR spectra for these two mixed EM+CT states closely resemble to the NR of the same cluster which can be approximated to the spectral shape of the EM enhancement mechanism, except for the enhancement of mode 6a. This means that for these particular complexes both EM and CT spectral shapes would be similar and both contributions would reinforce one to each other.

Therefore, the results here presented suggest that the largest EFs are achieved by synergy between the EM and CT contributions. In fact, since these hybrid states are bright, the large EFs can be readily understood from Albrecht A term showed in Eq. 5 and reproduced below for convenience:

$$I \propto |\alpha_{\rho\sigma}^{fi}|^2 = \left| \frac{\mu_\rho^{gk}(0)\mu_\sigma^{kg}(0)}{\hbar} \sum_m \frac{\langle \mathbf{n}^{f,g}|\mathbf{m}^k\rangle\langle \mathbf{m}^k|\mathbf{n}^{i,g}\rangle}{\omega_{km,gi} - \omega_{in} - i\gamma_k} \right|^2 \tag{6}$$

Under resonance conditions, $\omega_{km,gi} - \omega_{in} \approx 0$ and the denominator is roughly fixed by γ_k. Then, the transition polarizability components simply depend on the components of the ETDM and the FC factors. To achieve large intensities two conditions are required: i) the state must be bright because of the ETDM dependent factor and ii) large displacements along the normal coordinates with respect to the FC structure are needed. However, fulfilling simultaneously both conditions is in the general unattainable except for bright states localized in the adsorbate (RR mechanism): plasmon-like states in the metal can be very bright but they have small FC factors along the adsorbate degrees of freedom because the electronic density mainly changes on the metal cluster. This means that there is no shift between the ground and excited state potential energy surfaces along the adsorbate normal coordinates and, according to the harmonic oscillator selection rules, the second factor on Eq. 6 vanishes for Raman scattering. On the contrary, CT states have very large FC factors but their ETDM are close to zero because of the small orbital overlap. Therefore, only in this intermediate regime where the plasmon-like excitation and the CT are mixed it is possible to obtain large amplifications of the intensity through the A term, which dominates for these bright states.

It is worth to mention that this mixing of CT and plasmon-like states is simply the description of excited state coupling by adiabatic methods like TD-DFT when electronic states are very close in energy. This is

typically observed for bright states in excitonic systems and molecular aggregates and it is known that a localized picture with diabatic methods is more appropriated to analyse these effects,[66] suggesting that further methodological advances are necessary to completely describe the SERS-CT enhancement mechanism. At the same time, these results highlight that EC-SERS can be an ideal technique to study nonadiabatic effects both experimentally and computationally because the energy of the CT can be manipulated at will to couple and decouple them with bright states. This kind of electronic coupling due to the interaction among excited states is different to the vibronic coupling associated to normal coordinates described by the selection rules derived by Lombardi and Birke.[6] However, our results agree with their conclusions that all sources of the resonance Raman intensity in SERS, namely, EM, CT and RR, are not independent one of each other but coupled, and that the maximum SERS enhancements are in the vicinity of the surface plasmon, represented as localized excitations on the metal, and CT resonances.[6] Noteworthy, although in the cases here presented the source of coupling is different and the full system has no symmetry, we observed that in general only the totally symmetric fundamentals acquire intensity though the Albrecht A term above discussed, in line with the SERS selection rules. Some exceptions are found for S-$[Ag_{20}Py]^0$ and S-$[Ag_{20}Py]^0 - 20$, on which 8b band also acquires remarkable intensity. As shown in Figures S23 and S24, this is due to the lack of symmetry and the mixing of Py and $[Ag_{20}]^0$ orbitals.

In the SI we qualitatively analyze the contribution of other Albrecht terms by including Herzberg-Teller coupling, and these results show that additional intensity can be expected for the a_1 modes. Note that the absolute intensities cannot be trusted because the perturbative approach breaks down when the states are nearly degenerate. However, Herzberg-Teller can provide information on which modes are expected to gain additional intensity from the borrowing mechanism, although EFs cannot be estimated.

To conclude, we can only provide a rough lower bound for EF_{CT} of about 10^3-10^4. This is obtained by comparing the EF_{EM} when there is no coupling with the CT states, of 10^3 according to Figure 4 for systems like S-$[Ag_{20}Py]^0 + |E|$, with the mixed EF_{EM+CT} of 10^6-10^7 showed by S-$[Ag_{19}Py]^-$. This value for EF_{CT} agrees well with what reported in the literature,[67] although our estimates miss the contribution from vibronic coupling.

5.3 9,10-bis((E)-2-(pyridin-4-yl)vinyl)anthracene (BP4VA)

5.3.1 Selected bands and Vibrational Stark Effect

Next, we tested our computational model with BP4VA, a more complex molecule with a very different EC-SERS behaviour than Py and whose spectral relative intensities were previously studied by some of us.[30] Here we studied VSE effect and the estimation of EFs, while in the SI we also show the NR and RR spectra. Vibrational wavenumbers and intensities are almost insensitive to V_{el} and BP4VA possesses a bright local excitation on the visible range, allowing us to estimate EF_{RR}. In Figure S53 we reproduce the NR of the solid at 1064 nm and the experimental SERS at V_{el} = -0.6V. The most intense bands are a triad in the region 1500-1700 cm^{-1}, whose relative intensity changes with the excitation wavelength,[30] and several other bands are observed in the range between 900-1500 cm^{-1}, see Figures S6 and S7 for the assignment of the 12 modes selected here. Notice also that this molecule can show different stable conformers with very similar energy; however, their spectroscopic properties were found to be almost identical for different relative positions of the substituent on the anthracene moiety.[30] Therefore, we simply selected an *anti* arrangement for the (pyridyn-4-yl)vynyl substituents with respect to the anthracene plane and discussed only S-complexes. We considered the cases $|E|$ = 0, 10 when $q = \pm$ 1 and $|E|$ = 0, 20, 40 for q=0, all E in 10^{-4} a.u., see Sections S3.2 and S3.3 for details.

BP4VA is a much more complex system and differently to Py, the spectral bands may arise from the contribution of several fundamentals because of the dense manifold of vibrational states. Therefore, for our study of VSE we selected the most intense and better resolved experimental bands, namely, vynyl C=C stretching (Vy C=C str., 1627 cm^{-1}), pyridyl C=C stretching or 8a (Py C=C str., 1603 cm^{-1}), anthracyl C=C stretching (Anthr. C=C str., 1555 cm^{-1}), pyridyl and vynyl in-plane hydrogen bending (Py + Vy H-bend., 1200 cm^{-1}), anthracyl in-plane hydrogen bending (Anthr. H-bend., 1175 cm^{-1}) and anthracyl out-of-plane hydrogen bending (Anthr. H-OOP, 475 cm^{-1}). While we focused the discussion on these six modes, for completeness another six vibrations are presented in the SI (see Figure S7 and Section S3.2).

Because of the larger number of vibrational modes (144) and lack of symmetry on the system, we can expect that some of them are close in energy and mix differently as we modify E or the total charge q. Therefore, to isolate VSE from Duschinsky mixing, we took as reference the vibrational modes of the S-$[Ag_{20}BP4VA]^0$ cluster and computed the frequencies of these modes on all the other systems (see Section S1.6).

Figure 6 shows the potential-dependent wavenumbers of the selected bands. Our results accounting for Duschinsky effects reproduce very nicely the lack of sensitivity of the Raman shifts with V_{el} (q_{BP4VA} on calculations) for Vy C=C str., Anthr. C=C str., Anthr. H-bend. and Anthr. H-OOP modes, and also the

small changes on the Py + Vy H-bend. mode. Finally, the behaviour of the Py C=C str. mode is also reproduced in reasonable agreement, although some minor deviations are found in the most negative region. In general, the complexes S-[Ag_{20}BP4VA]$^{0}\pm$40 are out of the trend for several normal modes, suggesting once again that the charged clusters S-[Ag_{19}BP4VA]$^{\pm}$ with nearly the same q_{BP4VA} (see Table S9) fit better with the experimental trends. Namely, V_{el} between -0.1 and -0.2V would match with S-[Ag_{19}BP4VA]$^{+}$ while V_{el} = -1.0V is in better agreement with the S-[Ag_{19}BP4VA]$^{-}$ system according to our results and in line with what discussed for Py.

These results also suggest that VSE could have a very short range. Actually, only the nuclear motions with some contribution on the pyridyl group attached to the metal cluster show some dependence with V_{el}/q_{BP4VA} while those mainly localized on further groups like vynyl or anthracyl are almost insensitive to the electrochemical conditions. Such property is interesting and can be useful for the assignment of the experimental bands on other complex systems, a task not always simple even with the assistance of electronic structure calculations. However, this differentiated behaviour on the molecular groups can be due to the limited conjugation between them in BP4VA because of its intrinsic flexibility,[30] as the rotation of one group with respect to the next neighbour partially breaks conjugation, and further analysis in other systems would be useful to test this hypothesis.

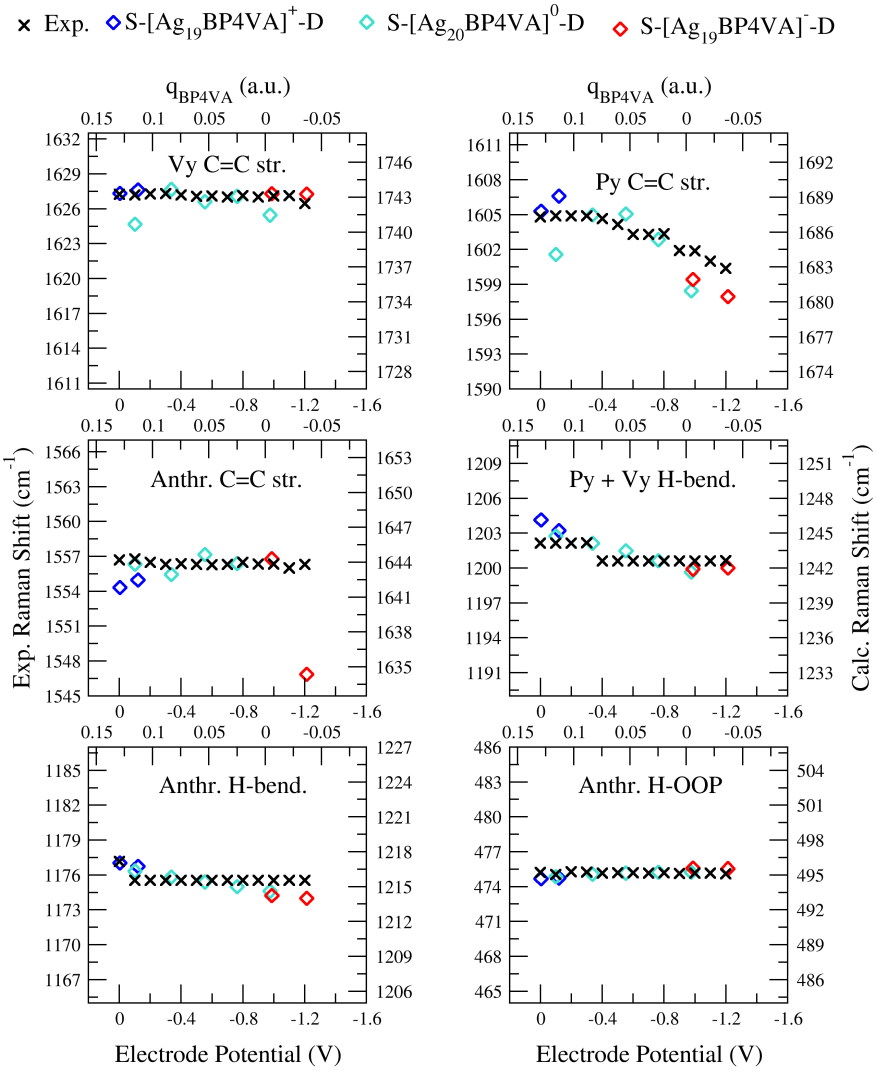

Figure 6: Raman shift electrode potential dependence of some BP4VA normal modes. The wavenumbers of S-[Ag_{20}BP4VA]^0 normal modes were projected into the other complexes with applied E and/or q, obtained by applying a Duschinsky transformation. The Y-axis represents the experimental (left) and calculated (right) Raman shift, and in all cases the range is 22 cm^{-1}. The calculated Raman shift range is selected to fit as best as possible with the experimental results. The X-axes show the experimental electrode potential applied (bottom) and the calculated charge on BP4VA (top). CAM-B3LYP-D3/6-31+G(2d,2p)/LANL2DZ level of theory. Excitation wavelength of 514.5 nm for experiments, data from Ref. 30

5.3.2 Spectra and Enhancement Factors

BP4VA EC-SERS spectra are also almost insensitive to V_{el}. The results obtained with our model agree with what previously reported with linear charged clusters and experimental results (see Section S3.4) and we focus here on the estimation of EFs. In general, the most intense spectra is due to the bright local excitation of BP4VA, i.e., RR mechanism. In some cases this state or the plasmon-like excitation of the metal mix with CT states, providing spectra with similar intensity to the RR contribution.

We can estimate the EFs by taking into account that the differential Raman cross section for isolated BP4VA is in the order of 10^{-29} cm^2/sr (Figure 53). Since for the RR of isolated BP4VA $d\sigma/d\Omega$ is in the order of 10^{-26} cm^2/sr, this results in an $EF_{RR} \sim 10^3$, in agreement with experimental observations in other chromophores absorbing in the visible range.[13] Our EF_{RR} for the metal-molecule hybrid systems shown in Figures S57 in the SI are in the same order. For the mixed EM+CT states, we obtain $EF_{EM+CT} \sim 10^5$. Therefore, in the most favourable case where all types of states (RR, EM and CT) are close in energy, EF up to 10^8 could be achieved, although this value may change depending on interference effects that can be either constructive or destructive.

6 Conclusions

In this paper we presented a computational model for EC-SERS and simultaneosly studied the three main V_{el}-dependent properties: vibrational Stark effect (VSE), relative intensities of the SERS spectra and EFs for each SERS contribution: chemical or nonresonant (CHEM) and resonance Raman with bright states of the adsorbate (RR), charge-transfer states (CT) and electromagnetic or plasmonic (EM). The model is tested with two molecules, one showing strong dependence on V_{el} (Py) and other with little sensibility to V_{el} (BP4VA). The surface excess of charge induced in the metal by V_{el} was included in the calculations by a dual approach. Charges on the adsorption site were explicit added as a positive or negative charge to the metal cluster, while the effect of other surface charges was implicitly reproduced as an external electric field, resulting on three sets of model complexes: $[Ag_{19}A]^+ + |E|$, $[Ag_{20}A]^0 \pm |E|$ and $[Ag_{19}A]^- - |E|$, with A = Py, BP4VA. To be able to compare among them, we selected as microspcopic analog to V_{el} the charge acquired by the adsorbate on each complex, q_A, which depends on the total charge q of the cluster to which the molecule is attached and the magnitude and direction of the external field E.

The model reproduced very nicely the VSE in terms of ranges and V_{el} dependence (q_A in our model) for the main spectral bands and allowed us to propose a qualitatively assignment of some electrochemical properties. Specifically, for the particular conditions of EC-SERS on silver electrode previously reported by our

group[28,30] it seems that $V_{PZC} \approx -0.6V$ and for $V_{el} \approx -1.0V$ the adsorption site apparently becomes negatively charged. This is supported by other experimental observations like the desorption of weakly bonded adsorbates for similar values of V_{el} in the same conditions,[61,62] suggesting that valuable electrochemical information can be obtained from EC-SERS studies. Nevertheless, to obtain more accurate estimations of V_{PZC} the theoretical model must include also the effects of solvent and electrolyte.

The soft changes on the SERS relative intensities of Py with V_{el} were also predicted well by either approximating the EM contribution to the SERS spectra to the NR of the metal clusters, or performing resonance Raman calculations with bright states of the metal cluster. The latter allowed to reproduce reasonably the ranges of V_{el} 0.0 to -0.3V and -0.6V to -1.2V but some limitations are detected and ascribed to the reduced number of Ag atoms in our clusters with respect to a true nanostructured electrode. The first approach based on NR of metal-molecule complexes provides a simple tool to analyze EC-SERS spectral shapes and identify possible resonances with specific states, like CT, by analysis of the differences with the experimental EC-SERS. However, with this approach the estimation of EFs is not possible. On the contrary, by analyzing the excited states of the metal-molecule system we identified that the coupling between bright local excitations and CT states can provide very large EFs, up to 10^7 for Py. This interaction between EM and CT states requires describing the electronic structure of the metal cluster at the quantum mechanical level.

However, this coupling is only observed for very specific electrochemical conditions in our model because of the small number of bright states on the tetrahedral cluster that can lend intensity to the dark CTs. This is very different from true metallic nanostructures which possess a dense manifold of bright states.[68,69] Therefore, it could be expected that the changes on the spectra with larger nanoparticles of less symmetry should be smoother than in our calculations, where the bright states of the metal and the CT decouple very fast and the calculated intensity falls down abruptly until another CT becomes closer in resonance with the metal local excitation. In addition, to properly introduce the electronic and vibronic coupling in the theoretical model, a nonadiabatic approach would be necessary but further methodological advances are required because they were only reported for small systems,[37] or using low-dimensionality models.[70] Progress in this direction are in development.[71] As an estimate, we used the perturbative Herzberg-Teller approach which suggested that further enhancement can be expected (but not limited to) a_1 modes of Py, in line with SERS selection rules,[6] and previous studies.[72]

For BP4VA, the EC-SERS spectra were dominated by the RR contribution due to a bright state of the molecule (RR mechanism), as already discussed in the literature.[30] Our results allowed us to estimate a EF_{RR} of 10^3. Mixed EM+CT states involving metal-to-molecule and molecule-to-metal processes were

detected in our calculations with $EF_{EM+CT} \approx 10^3 - 10^4$ and also RR+CT with molecule-to-metal charge transfer of weaker intensity, $EF_{RR+CT} \approx 10^2$, resulting from intensity borrowing of the bright state of BP4VA to the CT. The different types of CT provided additional intensity for some spectral bands, mainly those related to the pyridyl group like the experimental band ~ 1605 cm^{-1}.

The computational model for EC-SERS here proposed can be readily extended to other type of adsorbates with different type of anchoring groups, either monodentate like thiols or thioate,[73] bidentate as carboxilates or amides,[74] or to different cluster shapes[3] providing a systematic approach to simulate EC-SERS experiments. Nonadiabatic effects can be efficiently included in the model by using fragment-based approaches,[75,76] which permit to select the electronic states of interest and making feasible to use clusters like those here presented and that have proved to be reasonably good models for SERS systems.[29,67] In addition, the results here presented show that EC-SERS can be of potential interest to study nonadiabatic effect due to its capability to easily manipulate CT states energy at will both in experiments and calculations. Finally, this model for V_{el} in electronic structure calculations can be easily extended to metal-molecule-metal systems under the effect of an the applied bias and study electronic transport in molecular junctions or tip-enhanced Raman scatterig (TERS) with theoretical models already proposed in the literature, and of interest in fields like electrochemistry or molecular electronics.[77,78]

Supporting Information Available

Additional computational details. Additional results: adsorbate charges, wavenumber shifts, normal Raman spectra, Resonance Raman spectra and natural transition orbitals for all relevant states. This information is available free of charge via the Internet at http://pubs.acs.org

Acknowledgement

We thank Prof. Javier Cerezo (Universidad Autónoma de Madrid, Spain) and Dr. Fabrizio Santoro (Theoretical and Computational Chemistry Lab, ICCOM-CNR Pisa, Italy) for fruitful discussions on the computation of resonance Raman absolute intensities and for sharing the in development version of the code FCclasses3. D.A. acknowledges University of Málaga and Generalitat Valenciana/European Social Fund (APOSTD/2021/025) for postdoctoral contracts. F. G.-G. thanks University of Málaga for fundings (Predoctoral contract A2 I Plan Propio de Investigación, Transferencia y Divulgación Científica). We also thank University of Malaga SuperComputing and Bioinnovation Center (SCBI) for computational resources.

References

(1) Langer, J. et al. Present and future of surface-enhanced Raman scattering. *ACS Nano* **2019**, *14*, 28–117.

(2) Masiello, D. J.; Schatz, G. C. Many-body theory of surface-enhanced Raman scattering. *Phys. Rev. A* **2008**, *78*, 042505.

(3) Morton, S. M.; Jensen, L. Understanding the molecule-surface chemical coupling in SERS. *J. Am. Chem. Soc.* **2009**, *131*, 4090–4098.

(4) Fleischmann, M.; Hendra, P. J.; McQuillan, A. J. Raman spectra of pyridine adsorbed at a silver electrode. *Chem. Phys. Lett.* **1974**, *26*, 163–166.

(5) Albrecht, A. C. On the theory of Raman intensities. *J. Chem. Phys.* **1961**, *34*, 1476–1484.

(6) Lombardi, J. R.; Birke, R. L. A unified approach to surface-enhanced Raman spectroscopy. *J. Phys. Chem. C* **2008**, *112*, 5605–5617.

(7) Jensen, L.; Zhao, L.; Autschbach, J.; Schatz, G. Theory and method for calculating resonance Raman scattering from resonance polarizability derivatives. *J. Chem. Phys.* **2005**, *123*, 174110.

(8) Valley, N.; Jensen, L.; Autschbach, J.; Schatz, G. C. Theoretical studies of surface enhanced hyper-Raman spectroscopy: The chemical enhancement mechanism. *J. Chem. Phys.* **2010**, *133*, 054103.

(9) Valley, N.; Greeneltch, N.; Van Duyne, R. P.; Schatz, G. C. A look at the origin and magnitude of the chemical contribution to the enhancement mechanism of surface-enhanced Raman spectroscopy (SERS): theory and experiment. *J. Phys. Chem. Lett.* **2013**, *4*, 2599–2604.

(10) Harshan, A. K.; Bronson Jr, M. J.; Jensen, L. Local-field effects in linear response properties within a polarizable frozen density embedding method. *J. Chem. Theory Comput.* **2021**,

(11) Payton, J. L.; Morton, S. M.; Moore, J. E.; Jensen, L. A discrete interaction model/quantum mechanical method for simulating surface-enhanced Raman spectroscopy. *J. Chem. Phys.* **2012**, *136*, 214103.

(12) Becca, J. C.; Chen, X.; Jensen, L. A discrete interaction model/quantum mechanical method for simulating surface-enhanced Raman spectroscopy in solution. *J. Chem. Phys.* **2021**, *154*, 224705.

(13) Morton, S. M.; Silverstein, D. W.; Jensen, L. Theoretical studies of plasmonics using electronic structure methods. *Chem. Rev.* **2011**, *111*, 3962–3994.

(14) Kneipp, K.; Moskovits, M.; Kneipp, H. *Surface-enhanced Raman scattering: Physics and applications*; Springer Science & Business Media, 2006; Vol. 103.

(15) Le Ru, E. C.; Blackie, E.; Meyer, M.; Etchegoin, P. G. Surface enhanced Raman scattering enhancement factors: a comprehensive study. *J. Phys. Chem. C* **2007**, *111*, 13794–13803.

(16) Wu, D.-Y.; Li, J.-F.; Ren, B.; Tian, Z.-Q. Electrochemical surface-enhanced Raman spectroscopy of nanostructures. *Chem. Soc. Rev.* **2008**, *37*, 1025–1041.

(17) Willets, K. A. Probing nanoscale interfaces with electrochemical surface-enhanced Raman scattering. *Curr Opin Electrochem* **2019**, *13*, 18–24.

(18) Avila, F.; Ruano, C.; Lopez-Tocon, I.; Arenas, J. F.; Soto, J.; Otero, J. C. How the electrode potential controls the selection rules of the charge transfer mechanism of SERS. *ChemComm* **2011**, *47*, 4213–4215.

(19) Mohammadpour, M.; Khodabandeh, M. H.; Visscher, L.; Jamshidi, Z. Elucidation of charge-transfer SERS selection rules by considering the excited state properties and the role of electrode potential. *Phys. Chem. Chem. Phys.* **2017**, *19*, 7833–7843.

(20) Gieseking, R. L.; Ratner, M. A.; Schatz, G. C. Benchmarking semiempirical methods to compute electrochemical formal potentials. *J. Phys. Chem. A* **2018**, *122*, 6809–6818.

(21) Li, Y.; Doak, P.; Kronik, L.; Neaton, J. B.; Natelson, D. Voltage tuning of vibrational mode energies in single-molecule junctions. *Proc. Natl. Acad. Sci. USA* **2014**, *111*, 1282–1287.

(22) Ding, S.-Y.; Liu, B.-J.; Jiang, Q.-N.; Wu, D.-Y.; Ren, B.; Xu, X.; Tian, Z.-Q. Cations-modified cluster model for density-functional theory simulation of potential dependent Raman scattering from surface complex/electrode systems. *ChemComm* **2012**, *48*, 4962–4964.

(23) Lambert, D. K. Vibrational Stark effect of adsorbates at electrochemical interfaces. *Electrochim. Acta* **1996**, *41*, 623–630.

(24) Staffa, J. K.; Lorenz, L.; Stolarski, M.; Murgida, D. H.; Zebger, I.; Utesch, T.; Kozuch, J.; Hildebrandt, P. Determination of the local electric field at Au/SAM interfaces using the vibrational Stark effect. *J. Phys. Chem. C* **2017**, *121*, 22274–22285.

(25) Fried, S. D.; Boxer, S. G. Measuring electric fields and noncovalent interactions using the vibrational Stark effect. *Acc. Chem. Res.* **2015**, *48*, 998–1006.

(26) Fried, S. D.; Boxer, S. G. Electric fields and enzyme catalysis. *Annu. Rev. Biochem.* **2017**, *86*, 387–415.

(27) Li, Y.; Zolotavin, P.; Doak, P.; Kronik, L.; Neaton, J. B.; Natelson, D. Interplay of bias-driven charging and the vibrational Stark effect in molecular junctions. *Nano Lett.* **2016**, *16*, 1104–1109.

(28) Aranda, D.; Valdivia, S.; Soto, J.; López-Tocón, I.; Avila, F. J.; Otero, J. C. Theoretical Approaches for modeling the effect of the electrode potential in the SERS vibrational wavenumbers of pyridine adsorbed on a charged silver surface. *Front. Chem.* **2019**, *7*, 423.

(29) Zhao, L.; Jensen, L.; Schatz, G. C. Pyridine-Ag_{20} cluster: a model system for studying surface-enhanced Raman scattering. *J. Am. Chem. Soc.* **2006**, *128*, 2911–2919.

(30) Soto, J.; Imbarack, E.; López-Tocón, I.; Sánchez-Cortés, S.; Otero, J. C.; Leyton, P. Application of surface-enhanced resonance Raman scattering (SERS) to the study of organic functional materials: Electronic structure and charge transfer properties of 9, 10-bis ((E)-2-(pyridin-4-yl) vinyl) anthracene. *RSC Adv.* **2019**, *9*, 14511–14519.

(31) Neugebauer, J.; Reiher, M.; Kind, C.; Hess, B. A. Quantum chemical calculation of vibrational spectra of large molecules—Raman and IR spectra for buckminsterfullerene. *J. Comput. Chem.* **2002**, *23*, 895–910.

(32) Long, D. A. *The Raman effect: A unified treatment of the theory of Raman scattering by molecules*; Wiley, 2002.

(33) Neugebauer, J.; Baerends, E. J.; Nooijen, M. Vibronic coupling and double excitations in linear response time-dependent density functional calculations: Dipole-allowed states of N 2. *J. Chem. Phys.* **2004**, *121*, 6155–6166.

(34) Avila Ferrer, F. J.; Barone, V.; Cappelli, C.; Santoro, F. Duschinsky, Herzberg–Teller, and multiple electronic resonance interferential effects in resonance Raman spectra and excitation profiles. The case of pyrene. *J. Chem. Theory Comput.* **2013**, *9*, 3597–3611.

(35) Kramers, H. A.; Heisenberg, W. Über die streuung von strahlung durch atome. *Zeitschrift für Physik* **1925**, *31*, 681–708.

(36) Dirac, P. A. M. The quantum theory of dispersion. *Proc. Math. Phys. Eng.* **1927**, *114*, 710–728.

(37) Heather, R.; Metiu, H. Time-dependent theory of Raman scattering for systems with several excited electronic states: Application to a H+ 3 model system. *J. Chem. Phys.* **1989**, *90*, 6903–6915.

(38) Liu, Y.; Aranda, D.; Santoro, F. A computational study of the vibronic effects on the electronic spectra and the photophysics of aza[7]helicene. *Phys. Chem. Chem. Phys.* **2021**,

(39) Frisch, M. et al. Gaussian 16. 2016.

(40) Yanai, T.; Tew, D. P.; Handy, N. C. A new hybrid exchange–correlation functional using the Coulomb-attenuating method (CAM-B3LYP). *Chem. Phys. Lett.* **2004**, *393*, 51–57.

(41) Dichtel, W. R.; Hecht, S.; Fréchet, J. M. Functionally layered dendrimers: a new building block and its application to the synthesis of multichromophoric light-harvesting systems. *Organic Letters* **2005**, *7*, 4451–4454.

(42) Hariharan, P. C.; Pople, J. A. The influence of polarization functions on molecular orbital hydrogenation energies. *Theor. Chim. Acta* **1973**, *28*, 213–222.

(43) Hay, P. J.; Wadt, W. R. Ab initio effective core potentials for molecular calculations. Potentials for the transition metal atoms Sc to Hg. *J. Chem. Phys.* **1985**, *82*, 270–283.

(44) Hay, P. J.; Wadt, W. R. Ab initio effective core potentials for molecular calculations. Potentials for K to Au including the outermost core orbitals. *J. Chem. Phys.* **1985**, *82*, 299–310.

(45) Hay, P. J.; Wadt, W. R. Ab initio effective core potentials for molecular calculations. Potentials for K to Au including the outermost core orbitals. *J. Chem. Phys.* **1985**, *82*, 299–310.

(46) Grimme, S.; Antony, J.; Ehrlich, S.; Krieg, H. A consistent and accurate ab initio parametrization of density functional dispersion correction (DFT-D) for the 94 elements H-Pu. *J. Chem. Phys.* **2010**, *132*, 154104.

(47) Marenich, A. V.; Jerome, S. V.; Cramer, C. J.; Truhlar, D. G. Charge model 5: An extension of Hirshfeld population analysis for the accurate description of molecular interactions in gaseous and condensed phases. *J. Chem. Theory Comput.* **2012**, *8*, 527–541.

(48) Santoro, F.; Cerezo, J. $\mathcal{FC}classes3$, a code for vibronic calculations. Available upon request. 2019.

(49) Santoro, F.; Cappelli, C.; Barone, V. Effective time-independent calculations of vibrational resonance Raman spectra of isolated and solvated molecules including Duschinsky and Herzberg–Teller effects. *J. Chem. Theory Comput.* **2011**, *7*, 1824–1839.

(50) Ferrer, F. J. A.; Santoro, F. Comparison of vertical and adiabatic harmonic approaches for the calculation of the vibrational structure of electronic spectra. *Phys. Chem. Chem. Phys.* **2012**, *14*, 13549–13563.

(51) Santoro, F.; Improta, R.; Lami, A.; Bloino, J.; Barone, V. Effective method to compute Franck-Condon integrals for optical spectra of large molecules in solution. *J. Chem. Phys.* **2007**, *126*, 084509.

(52) Santoro, F.; Lami, A.; Improta, R.; Bloino, J.; Barone, V. Effective method for the computation of optical spectra of large molecules at finite temperature including the Duschinsky and Herzberg–Teller effect: the Q_x band of porphyrin as a case study. *J. Chem. Phys.* **2008**, *128*, 224311.

(53) Baiardi, A.; Bloino, J.; Barone, V. General time-dependent approach to vibronic spectroscopy including Franck-Condon, Herzberg-Teller, and Duschinsky effects. *J. Chem. Theory Comput.* **2013**, *9*, 4097–4115.

(54) Cerezo, J.; Mazzeo, G.; Longhi, G.; Abbate, S.; Santoro, F. Quantum-classical calculation of vibronic spectra along a reaction path: the case of the ECD of easily interconvertible conformers with opposite chiral responses. *J. Phys. Chem. Lett.* **2016**, *7*, 4891–4897.

(55) Cerezo, J.; Aranda, D.; Avila Ferrer, F. J.; Prampolini, G.; Santoro, F. Adiabatic-molecular dynamics generalized vertical hessian approach: a mixed quantum classical method to compute electronic spectra of flexible molecules in the condensed phase. *J. Chem. Theory Comput.* **2019**, *16*, 1215–1231.

(56) Román-Pérez, J.; López-Tocón, I.; Castro, J.; Arenas, J.; Soto, J.; Otero, J. The electronic structure of metal–molecule hybrids in charged interfaces: surface-enhanced Raman selection rules derived from plasmon-like resonances. *Phys. Chem. Chem. Phys.* **2015**, *17*, 2326–2329.

(57) Arenas, J. F.; López Tocón, I.; Otero, J. C.; Marcos, J. I. Charge transfer processes in surface-enhanced Raman scattering. Franck-Condon active vibrations of pyridine. *J. Phys. Chem* **1996**, *100*, 9254–9261.

(58) Wilson Jr, E. B. Calculation of vibrational isotope effect in polyatomic molecules by a perturbation method. *Phys. Rev.* **1934**, *45*, 427.

(59) Chen, Y.-X.; Otto, A. Electronic effects in SERS by liquid water. *J. Raman Spectrosc.* **2005**, *36*, 736–747.

(60) Gómez, R.; Climent, V.; Feliu, J. M.; Weaver, M. J. Dependence of the potential of zero charge of stepped platinum (111) electrodes on the oriented step-edge density: Electrochemical implications and comparison with work function behavior. *J. Phys. Chem. B* **2000**, *104*, 597–605.

(61) Soto, J.; Fernández, D.; Centeno, S.; López Tocón, I.; Otero, J. Surface orientation of pyrazine adsorbed on silver from the surface-enhanced Raman scattering recorded at different electrode potentials. *Langmuir* **2002**, *18*, 3100–3104.

(62) Lopez-Ramirez, M. R.; Ruano, C.; Castro, J. L.; Arenas, J. F.; Soto, J.; Otero, J. C. Surface-enhanced Raman scattering of benzoate anion adsorbed on silver nanoclusters: Evidence of the transient formation of the radical dianion. *J. Phys. Chem. C* **2010**, *114*, 7666–7672.

(63) Innes, K.; Byrne, J.; Ross, I.-G. Electronic states of azabenzenes: A critical review. *J. Mol. Spectrosc.* **1967**, *22*, 125–147.

(64) Martin, R. L. Natural transition orbitals. *J. Chem. Phys.* **2003**, *118*, 4775–4777.

(65) Huang, Q.; Lin, X.; Yang, Z.; Hu, J.; Tian, Z. An investigation of the adsorption of pyrazine and pyridine on nickel electrodes by in situ surface-enhanced Raman spectroscopy. *J. Electroanal. Chem.* **2004**, *563*, 121–131.

(66) Hestand, N. J.; Spano, F. C. Expanded theory of H-and J-molecular aggregates: the effects of vibronic coupling and intermolecular charge transfer. *Chem. Rev.* **2018**, *118*, 7069–7163.

(67) Jensen, L.; Aikens, C. M.; Schatz, G. C. Electronic structure methods for studying surface-enhanced Raman scattering. *Chem. Soc. Rev.* **2008**, *37*, 1061–1073.

(68) Aikens, C. M.; Li, S.; Schatz, G. C. From discrete electronic states to plasmons: TD-DFT optical absorption properties of Ag_n (n= 10, 20, 35, 56, 84, 120) tetrahedral clusters. *J. Phys. Chem. C* **2008**, *112*, 11272–11279.

(69) Jensen, L. L.; Jensen, L. Atomistic electrodynamics model for optical properties of silver nanoclusters. *J. Phys. Chem. C* **2009**, *113*, 15182–15190.

(70) Stock, G.; Woywod, C.; Domcke, W.; Swinney, T.; Hudson, B. S. Resonance Raman spectroscopy of the S 1 and S 2 states of pyrazine: Experiment and first principles calculation of spectra. *J. Chem. Phys.* **1995**, *103*, 6851–6860.

(71) Xu, Q.; Aranda, D.; Martha, Y. J.; Liu, Y.; Wang, M.; Cerezo, J.; Improta, R.; Santoro, F. Nonadiabatic vibrational resonance Raman spectra from quantum dynamics propagations with LVC models. Application to thymine. *J. Phys. Chem. A, Accepted* **2022**,

(72) Liu, L.; Chen, D.; Ma, H.; Liang, W. Spectral characteristics of chemical enhancement on SERS of benzene-like derivatives: Franck–Condon and Herzberg–Teller contributions. *J. Phys. Chem. C* **2015**, *119*, 27609–27619.

(73) Sun, Y.; Song, W.; Zhu, X.; Zhang, R.; Pang, Q.; Zhang, Z.; Yang, H. Electrochemical and in situ SERS spectroelectrochemical investigations of 4-methyl-4H-1, 2, 4-triazole-3-thiol monolayers at a silver electrode. *J. Raman Spectrosc.* **2009**, *40*, 1306–1311.

(74) Anto, P.; Panicker, C. Y.; Varghese, H. T.; Philip, D. Potential-dependent SERS profile of orthanilic acid on silver electrode. *J. Raman Spectrosc.* **2006**, *37*, 1265–1271.

(75) Green, J. A.; Yaghoubi Jouybari, M.; Asha, H.; Santoro, F.; Improta, R. Fragment diabatization linear vibronic coupling Model for quantum dynamics of multichromophoric systems: population of the

charge-transfer state in the photoexcited guanine–cytosine pair. *J. Chem. Theory Comput.* **2021**, *17*, 4660–4674.

(76) Wang, Y.-C.; Feng, S.; Liang, W.; Zhao, Y. Electronic couplings for photoinduced charge transfer and excitation energy transfer based on fragment particle–hole densities. *J. Phys. Chem. Lett.* **2021**, *12*, 1032–1039.

(77) Zhao, X.; Liu, S.; Li, Y.; Chen, M. DFT study of chemical mechanism of pre-SERS spectra in Pyrazine–metal complex and metal–Pyrazine–metal junction. *Spectrochim. Acta A Mol. Biomol. Spectrosc.* **2010**, *75*, 794–798.

(78) Jamshidi, Z.; Asadi-Aghbolaghi, N.; Morad, R.; Mahmoudi, E.; Sen, S.; Maaza, M.; Visscher, L. Comparing the nature of quantum plasmonic excitations for closely spaced silver and gold dimers. *J. Chem. Phys.* **2022**, *156*, 074102.

Graphical TOC Entry

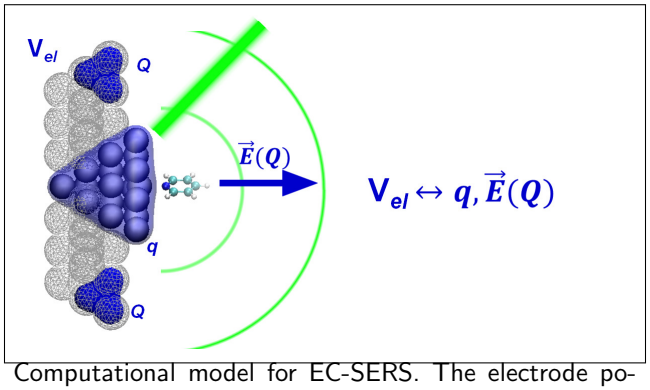

Computational model for EC-SERS. The electrode potential V_{el} is reproduced by the charge of the adsorption site q and an electric field $\vec{E}$ representing the effect of nearby surface charges Q.